


**Chaotic precession of antiferromagnetic domain walls**Yangyi Chen,<sup>1,2,\*</sup> Xu Ge,<sup>1,\*</sup> Wei Luo,<sup>1</sup> Shiheng Liang,<sup>3</sup> Xiaofei Yang,<sup>1</sup> Long You<sup>1</sup>,,<sup>1</sup> Yue Zhang<sup>1,†</sup>,,<sup>1,†</sup> and Zhe Yuan<sup>4,‡</sup><sup>1</sup>*School of Integrated Circuits, Huazhong University of Science and Technology, Wuhan 430074, China*<sup>2</sup>*State Key Laboratory of Precision Measurement Technology and Instruments, Department of Precision Instrument, Tsinghua University, Beijing 100084, China*<sup>3</sup>*Faculty of Physics and Electronic Science, Hubei University, Wuhan 430062, China*<sup>4</sup>*Center for Advanced Quantum Studies and Department of Physics, Beijing Normal University, Beijing 100875, China*

(Received 15 July 2022; revised 2 October 2022; accepted 10 January 2023; published 17 January 2023)

In contrast with extensive investigations on the translation of domain walls (DWs) in antiferromagnetic (AFM) materials, the precessional motion of an AFM DW is seldom concerned partly because of the lack of an effective driving method. In this Letter, we show that under an alternating spin-polarized current with polarization along the AFM anisotropy axis, an AFM DW can be excited to precess. Especially, chaotic precession occurs at a moderate interfacial Dzyaloshinskii-Moriya interaction (DMI), which contributes to a nonlinear term in the dynamic equation of DW precession. Crisis-induced intermittent chaos appears when the current density is higher than a critical value. This Letter not only paves a way to unravel the rich dynamics of a current-induced AFM texture but also provides guidelines for developing ultrafast spintronic devices to exploit the nonlinear chaotic magnetization dynamics with promising applications.

DOI: [10.1103/PhysRevB.107.L020405](https://doi.org/10.1103/PhysRevB.107.L020405)

**Introduction.** Chaos is deterministic nonlinear dynamics that is sensitive to the variation of initial conditions and has attracted extensive investigations owing to its wide existence in nature and applications in numerous fields [1–6]. Typical applications of chaos include secure communication [2] and the detection of extremely weak signals [3,4]. Very recently, promising applications of chaos have been proposed in neuro-morphic computing, such as seeking a global optimal solution in combinatorial optimization problems [5,6].

A spintronic device can exhibit chaotic magnetization dynamics due to the inherent nonlinearity in the dynamic equation. For example, chaotic magnetization precession is observed in spin-torque or spin Hall nano-oscillators [7–14]. The strong exchange coupling in antiferromagnetic (AFM) materials leads to spin dynamics in the terahertz regime [15,16] including ultrafast chaotic spin precession [17]. Nevertheless, an AFM material with a uniform magnetization requires a strong driving force for breaking the antiparallel spin alignment stabilized by an exchange field [18]. In recent decades, the magnetization dynamics of AFM textures, such as domain walls (DWs), skyrmions, vortices, and bimerons, has attracted broad attention [19–22] because AFM textures can be driven by applying an electrical current or a voltage exhibiting both interesting dynamical behaviors and potential applications [23–26]. As an example, current-driven ultrafast AFM DW translation was achieved with a relativistic velocity larger than 1 km/s in a heavy metal/AFM bilayer [24,27]. Chaotic AFM texture translation has also been predicted un-

der an alternating spin current in the presence of nonlinear boundary-induced force [28,29].

So far, most studies of the DW dynamics in AFM materials were focused on translational motion. However, precessional motion is another dynamical mode for magnetic textures but less attention has been paid to this mode. Precessional motion is absent at uniform translations of AFM textures and can be entangled with their acceleration in a complex manner [24,30,31]. To reveal the dynamical properties of the precessional mode for AFM textures, one needs a special excitation to prevent translational motion.

In this Letter, we demonstrate that the precessional motion of an AFM DW can be triggered by a spin-polarized electrical current with a very low current density via conventional spin-transfer torque (STT). In this case the translational motion of the AFM DW is suppressed and a static DW location is sustained. In particular, the DW precession exhibits intermittent chaotic behaviors at a moderate interfacial Dzyaloshinskii-Moriya interaction (DMI), which contributes to a nonlinear term in the dynamic equation of the DW precession. Our results unravel rich behaviors in the precessional dynamics of an AFM DW, and the discovered chaotic characteristics open another route for the applications of nanoscale spintronic devices with a high speed of processing.

**STT-driven AFM DW motion.** We considered a spin-valve-like structure composed by a free AFM layer and a pinned ferromagnetic (FM) layer separated by a nonmagnetic metal layer, as sketched in Fig. 1(a). The magnetization of the FM layer is fixed along the  $z$  direction. The AFM layer consists of two sublattices  $A$  and  $B$ , in which a one-dimensional (1D) Néel-type chiral DW along the  $x$  direction is stabilized by an interfacial DMI. This device configuration is experimentally feasible for investigating magnetization dynamics driven by spin-polarized currents [32,33]. When an electrical current

\*These authors contributed equally to this work.

†yue-zhang@hust.edu.cn

‡zyuan@bnu.edu.cn

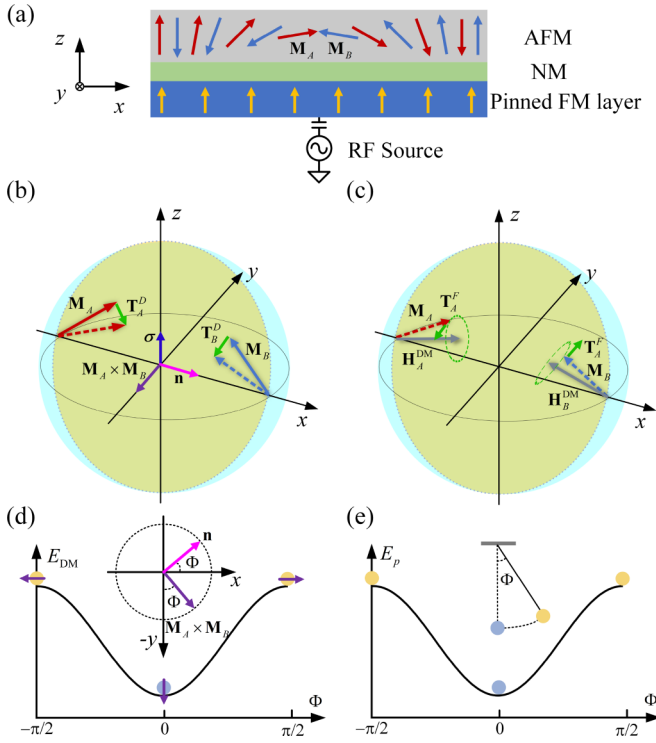


FIG. 1. (a) Schematic of the spin-valve-like structure for exciting the precessional motion of a Néel-type DW in the top AFM layer by injecting an alternating spin-polarized current from the bottom FM layer. The pinned FM layer has a fixed magnetization (yellow arrows) along the  $z$  axis.  $\mathbf{M}_A$  and  $\mathbf{M}_B$  denote the magnetic moments in the two sublattices  $A$  and  $B$  at the DW center. (b) Rotation of  $\mathbf{M}_A$  and  $\mathbf{M}_B$  under dampinglike torques ( $\mathbf{T}_A^D$  and  $\mathbf{T}_B^D$ ) as indicated by the green arrows. When  $\mathbf{M}_A$  and  $\mathbf{M}_B$  are lying in the  $xz$  plane, the Néel vector  $\mathbf{n}$  (magenta arrow) is along  $x$  and  $\mathbf{M}_A \times \mathbf{M}_B$  (purple arrow) is along  $-y$ . (c) Precession of  $\mathbf{M}_A$  and  $\mathbf{M}_B$  under a fieldlike torque of DMI ( $\mathbf{T}_A^F$  and  $\mathbf{T}_B^F$ ). Here, the gray and green arrows represent the effective field and the fieldlike torque of DMI, respectively. The light green areas in (b) and (c) indicate the  $xz$  plane. (d) Precession of  $\mathbf{M}_A$  and  $\mathbf{M}_B$  results in the rotations of  $\mathbf{M}_A \times \mathbf{M}_B$  and  $\mathbf{n}$  in the  $xy$  plane, which in turn changes the DMI energy proportional to  $\cos \Phi$ . Here,  $\Phi$  is the angle between  $\mathbf{M}_A \times \mathbf{M}_B$  and  $-y$ . The Néel vector remains perpendicular to  $\mathbf{M}_A$  and  $\mathbf{M}_B$  with the angle  $\Phi$  from  $x$ . The energy profile of AFM DW precession under an alternating spin-polarized current (d) is analogous to that of a pendulum under an alternating driving force (e).

passes through the pinned FM layer, a spin-polarized current with its polarization along  $z$  is injected into the AFM DW via the spacer layer. Note that the current polarization is always collinear with the local magnetic moments in the AFM material outside of the DW, where the STT does not excite bulk spin waves [16]. Moreover, the current-density threshold of exciting bulk spin waves is approximately  $10^8$  A/cm<sup>2</sup>, which is two orders of magnitude larger than the current density range in this work. Therefore, the bulk spin waves can be safely neglected.

To characterize DW precession, we focus on the two magnetic moments in sublattices  $A$  and  $B$  at the DW center without loss of generality, which are marked as  $\mathbf{M}_A$  and  $\mathbf{M}_B$  in Fig. 1(a). Under a dampinglike STT  $\mathbf{T}_{A(B)}^D \propto \mathbf{M}_{A(B)} \times (\mathbf{M}_{A(B)} \times \hat{z})$ , the magnetic moments  $\mathbf{M}_A$  and  $\mathbf{M}_B$  both rotate

in the  $xz$  plane [the light green areas in Figs. 1(b) and 1(c)]. A dampinglike STT breaks the DW stability while the fieldlike torques drive the local magnetic moments  $\mathbf{M}_A$  and  $\mathbf{M}_B$  to precess about the total effective field including the exchange field, anisotropy field, DMI field, and current-induced field.

For a chiral Néel DW with magnetic moments lying inside the  $xz$  plane, the effective fields due to DMI exerting on  $\mathbf{M}_A$  and  $\mathbf{M}_B$  ( $\mathbf{H}_A^{\text{DM}}$  and  $\mathbf{H}_B^{\text{DM}}$ ) are also in the  $xz$  plane and have a mirror symmetry about the  $z$  axis. These torques result in the precession of  $\mathbf{M}_A$  and  $\mathbf{M}_B$  with the same amplitude but opposite chirality, as schematically illustrated in Fig. 1(c). Consequently, the vector  $\mathbf{M}_A \times \mathbf{M}_B$  rotates in the  $xy$  plane with the equilibrium direction along  $-y$ , because the DMI energy depends on this vector as  $E_{\text{DM}} = -D\hat{y} \cdot (\mathbf{M}_A \times \mathbf{M}_B)$  [34,35]. This energy profile, depending on the vector  $\mathbf{M}_A \times \mathbf{M}_B$ , is analogous to the gravitational potential energy of a pendulum that depends on the angle deviating from its equilibrium, which is shown in Figs. 1(d) and 1(e) for comparison.

The above analysis reveals the possibility for AFM DW precession under an alternating spin-polarized current in combination with DMI. To quantitatively describe the AFM DW dynamics, we derived the dynamic equation of the total magnetization  $\mathbf{m} = \mathbf{M}_A + \mathbf{M}_B$  and the Néel order parameter  $\mathbf{n} = (\mathbf{M}_A - \mathbf{M}_B)/2M_s$ , where  $M_s$  is the saturation magnetization of each sublattice. For the 1D AFM DW shown in Fig. 1(a), we write the leading-order free energy in the continuum approximation as

$$H = S_{\perp} \int \left[ \frac{a}{2} \mathbf{m}^2 + \frac{A}{2} \mathbf{n}^2 + L \mathbf{m} \cdot \mathbf{n}' - \frac{K}{2} n_z^2 + \frac{D}{2} \hat{y} \cdot (\mathbf{n} \times \mathbf{n}') \right] dx. \quad (1)$$

Here,  $S_{\perp}$  is the cross-sectional area of the AFM material and the prime denotes the spatial derivative with respect to  $x$ .  $a$ ,  $A$ ,  $K$ , and  $D$  are the homogeneous exchange, exchange stiffness, uniaxial anisotropy, and DMI coefficients, respectively. The sign and magnitude of the interfacial DMI depend on the composition above and below the magnetic layer and can be tuned in a wide range [36].

Under the spin-polarized current density  $J$  with its polarization  $P$ , the dynamic equations of  $\mathbf{m}$  and  $\mathbf{n}$  can be expressed as [24]

$$\frac{\dot{\mathbf{n}}}{\gamma} = \left( \mathbf{f}_m - \frac{G_1 \dot{\mathbf{m}}}{\gamma} \right) \times \mathbf{n} + \frac{T_D}{l} \mathbf{n} \times (\mathbf{m} \times \hat{z}) + T_F (\mathbf{n} \times \hat{z}), \quad (2)$$

$$\frac{\dot{\mathbf{m}}}{\gamma} = \left( \mathbf{f}_n - \frac{G_2 \dot{\mathbf{n}}}{\gamma} \right) \times \mathbf{n} + T_D l \mathbf{n} \times (\mathbf{n} \times \hat{z}) + T_F (\mathbf{m} \times \hat{z}), \quad (3)$$

where the overdot indicates the time derivative and  $\gamma = 1.76 \times 10^{11}$  rad/(s T) is the gyromagnetic ratio.  $\mathbf{f}_m = -a\mathbf{m} - L\mathbf{m}'$  and  $\mathbf{f}_n = A\mathbf{n}'' + L\mathbf{m}' + Kn_z\hat{z} + D\hat{y} \times \mathbf{n}'$  are the effective fields exerted on  $\mathbf{m}$  and  $\mathbf{n}$ , respectively. We define  $l = |\mathbf{M}_A - \mathbf{M}_B|$ , which is close to  $2M_s$  with strong exchange coupling.  $G_1 = \alpha/l$  and  $G_2 = \alpha l$  are the effective damping coefficients for  $\mathbf{m}$  and  $\mathbf{n}$ , respectively, where  $\alpha$  is the Gilbert damping. The strength of the dampinglike STT is  $T_D = \mu_B P J / \gamma e M_s t_z$  with  $\mu_B$  the Bohr magneton and  $e$  the electron charge.  $P = 0.48$  is

the spin polarization for Pt/Co [37],  $M_s = 5.05 \times 10^5$  A/m is chosen for  $L1_0$ -MnPt [38], and  $t_z = 0.4$  nm is the thickness of the AFM layer.  $T_F$  is the strength of the fieldlike STT, which does not contribute to the DW precession (see Sec. S-I in the Supplemental Material [39]).

Equations (2) and (3) can be simplified as

$$\begin{aligned} \ddot{\mathbf{n}} + a\gamma G_2 \dot{\mathbf{n}} - a\gamma^2 (A^* \mathbf{n}'' + Kn_z \hat{z} + D\hat{y} \times \mathbf{n}') \\ + a\gamma^2 T_D l \mathbf{n} \times \hat{z} = \mathbf{0}, \end{aligned} \quad (4)$$

where  $A^* \equiv A - L^2/a$  is the effective exchange constant including the parity-breaking term [51]. We rewrite  $\mathbf{n} = (\sin \theta \cos \Phi, \sin \theta \sin \Phi, \cos \theta)$  in a spherical coordinate system with  $\theta$  and  $\Phi$  the polar and azimuthal angles, respectively. Using the collective coordinates for a Walker-type DW [15], the polar angle can be expressed in terms of the DW center  $X$  and its width  $\lambda$ . For simplicity, we assume that the Walker-type DW structure and its width  $\lambda$  are well maintained during the precession and this assumption is verified by atomistic simulation (see Sec. S-II of the Supplemental Material [39]). Taking the scalar product of Eq. (4) with  $\partial \mathbf{n} / \partial X$  and  $\partial \mathbf{n} / \partial \Phi$ , respectively, and integrating over space, we finally obtain the Thiele equations,

$$\ddot{X} + a\gamma G_2 \dot{X} = 0, \quad (5)$$

$$\ddot{\Phi} + a\gamma G_2 \dot{\Phi} - \frac{\pi}{4\lambda} a\gamma^2 D \sin \Phi = a\gamma^2 T_D l. \quad (6)$$

In previous studies of the dynamics of AFM textures, the driving force was generally acted on  $X$  while  $\Phi$  was usually assumed to be constant [24]. Therefore, most attention was paid to the translational motion instead of the DW precession. However, under a spin-polarized current with its polarization along the AFM anisotropy axis, the STT term appears in the dynamic equation of  $\Phi$  instead of  $X$ ; see Eqs. (5) and (6). It is worth noticing that Eq. (6) has the same form as the dynamic equation of a classical pendulum. Therefore, the equivalence between the precessional motion of an AFM DW and the classical pendulum is demonstrated in their energy profiles [Figs. 1(d) and 1(e)] and the dynamical equations [Eq. (6)]. Since a classical pendulum can exhibit chaotic oscillation under an alternating driving force, the chaotic DW precession can be achieved under an alternating spin-polarized current.

*Chaotic precession of AFM DWs.* To verify our prediction, we numerically solved Eq. (6) using the fourth-order Runge-Kutta method with a time step of 0.01 ps. Under an alternating current with a frequency  $f_0 = 100$  GHz, the representative numerical results are plotted in Fig. 2. At  $\alpha = 2 \times 10^{-2}$ , the DW exhibits a regular precession, as shown in Fig. 2(a). In addition to the driving frequency  $f_0$ , weaker precessions at higher frequencies are also seen in the spectrum [Fig. 2(b)]. These higher-order signals originate from the nonlinear terms in the Taylor expansion of  $\sin \Phi$  in Eq. (6). At a small damping  $\alpha = 2 \times 10^{-3}$ ,  $\Phi(t)$  does not exhibit a periodic motion and the trajectory in the phase diagram fails to close after a long time ( $>800$  ps), as shown in Fig. 2(c). Unlike the periodic precession, there is no sharp peak in the spectrum of  $\Phi$ ; see Fig. 2(d). In addition, the power spectrum of  $d\Phi/dt$  shows a power law with an exponent of approximately  $-2$  in the frequency range between  $0.1f_0$  and  $10f_0$  [inset of Fig. 2(d)], which is a signature of intermittent chaos due to the random

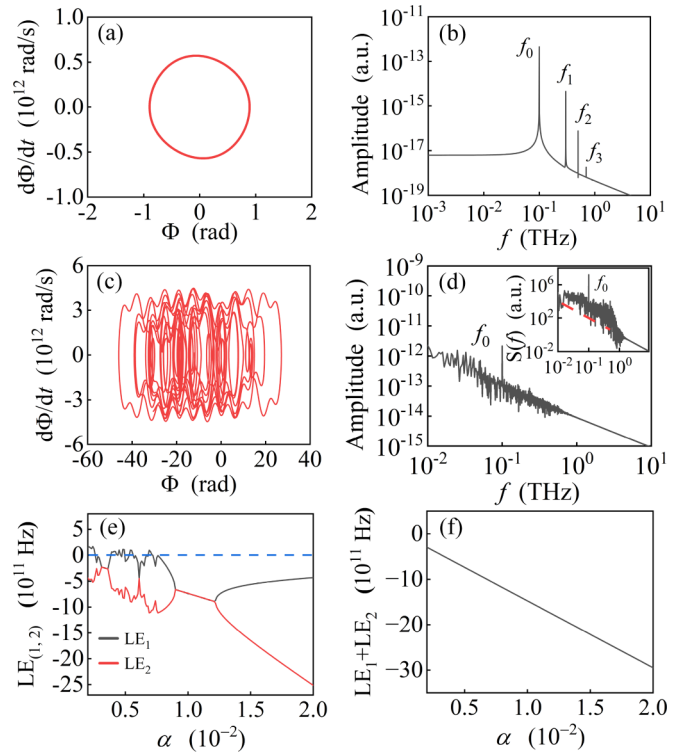


FIG. 2. Trajectories in phase portraits  $d\Phi/dt$  vs  $\Phi$  and the spectra of  $\Phi$  at  $\alpha = 2 \times 10^{-2}$  [(a) and (b)] and  $\alpha = 2 \times 10^{-3}$  [(c) and (d)] for  $D = -0.174$  mJ/m<sup>2</sup> and  $J = 1 \times 10^{11}$  A/m<sup>2</sup>.  $f_0$  denotes the frequency of the alternating spin-polarized current.  $f_1 = 3f_0$ ,  $f_2 = 5f_0$ , and  $f_3 = 7f_0$  indicate the higher-order precessional frequency due to the nonlinear DMI. The inset of (d) is the power spectrum of  $d\Phi/dt$  in a log-log scale and the red dashed line denotes a logarithmic slope  $-2$ . Calculated Lyapunov exponents  $LE_1$  and  $LE_2$  (e) and the sum of  $LE_1$  and  $LE_2$  (f) as a function of the damping coefficient  $\alpha$ .

state hopping model [52,53]. All these features consistently indicate that the AFM DW shows a chaotic precession at a small  $\alpha$  driven by the spin-polarized current. The periodic precession and chaotic precession obtained by solving Eq. (6) is further confirmed by the atomistic simulation of spin dynamics, as presented in detail in Sec. S-II of the Supplemental Material [39].

To understand the appearance of chaos at low damping, we calculated the Lyapunov exponents (LEs) defined as [28]

$$LE_i = \lim_{t \rightarrow \infty} \frac{1}{t} \ln \frac{\|\delta\Phi_t^i\|}{\|\delta\Phi_0^i\|}. \quad (7)$$

Here,  $\|\delta\Phi_t^i\|$  is the distance between two closed trajectories at time  $t$  and  $\|\delta\Phi_0^i\|$  is the initial distance at  $t = 0$ .  $i = 1, 2$ , and  $3$  stand for  $\Phi$ ,  $d\Phi/dt$ , and  $t$ , respectively; see the details in Sec. S-III of the Supplemental Material [39]. A positive  $LE_1$  indicates chaotic dynamics with an exponential increase of the distance between two trajectories for any nonzero  $\|\delta\Phi_0^i\|$ . The relation  $LE_1 + LE_2 = -a\gamma a l$  holds [39] and is explicitly verified in Fig. 2(f). Although the sum of  $LE_1$  and  $LE_2$  remains negative, a small  $\alpha$  provides a larger probability for the appearance of a positive  $LE_1$  to achieve the chaotic precession, as shown in Fig. 2(e).



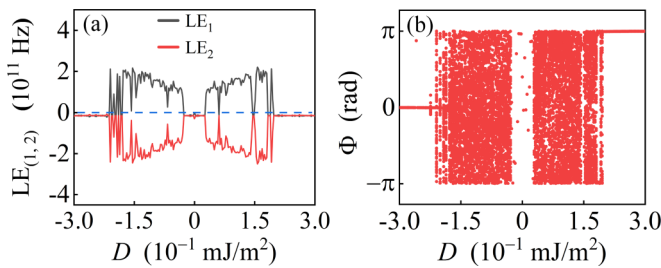


FIG. 3. (a) Lyapunov exponents  $LE_1$  and  $LE_2$  and (b) bifurcation diagram as a function of the DMI strength  $D$ .

**Influence of DMI and current density.** The dynamical equation (6) suggests that the DMI strength and current density play a significant role in the DW precession in addition to the damping coefficient. Figure 3(a) shows  $LE_1$  and  $LE_2$  as a function of the DMI strength  $D$ .  $LE_1$  is negative at small and large DMI, indicating the absence of chaotic DW precession. DMI can be regarded as the restoring force in the DW precession in analog to the gravitational force in a classical pendulum. Under a large enough DMI, the strong restoring force suppresses the amplitude of DW precession  $\Phi$ . Then  $\sin \Phi \approx \Phi$  becomes a good approximation while the nonlinearity of Eq. (6) disappears [54], resulting in periodic DW precession. At very weak DMI, the nonlinear term in Eq. (6) becomes negligible. Only at moderate DMI is the calculated  $LE_1$  positive and chaotic DW precession occurs. Chaotic DW precession can also be verified from the bifurcation diagram; see Fig. 3(b). Here, we collected  $\Phi$  at a series of moments with an interval of the period of the driving current. Only a single  $\Phi$  appears under either weak or strong DMI, but many different  $\Phi$  emerge at moderate DMI, confirming chaotic DW precession.

Chaotic DW precession is manipulated by a dampinglike torque via the spin-polarized current density and the resulting intermittent chaos exhibits alternating periodic and aperiodic dynamics. This can be induced by the collision of a chaotic attractor with the basin boundary of the attractor (crisis) in a system with multiple attractors [39,55]. Here, the basin describes the collection of initial conditions that leads to a long-term behavior approaching an attractor. Under typical crisis-induced intermittent chaos, the trajectory in the phase portrait would wander between different attractors.

When the current density  $J$  exceeds a critical value  $J_{c1} = 4 \times 10^{10}$  A/m<sup>2</sup>, there are two running attractors with an average positive or negative angular velocity, as shown by the blue and green lines in Figs. 4(a) and 4(b). They are also displayed by the white and pink regions in Figs. 4(d) and 4(e). At  $J = 4.9 \times 10^{10}$  A/m<sup>2</sup>, the attractors were period-2, and the Poincaré sections at  $2\pi f_0 t = 0 \pmod{2\pi}$  were individual dots located within different basins; see Fig. 4(d). If  $J$  is larger than another critical value  $J_{c2} = 4.98 \times 10^{10}$  A/m<sup>2</sup>, the attractors became chaotic, and the Poincaré sections became continuous lines but are still confined in their own attractors, as shown in Figs. 4(b) and 4(e). When  $J$  is further increased to exceed the third critical value  $J_{c3} = 5.04 \times 10^{10}$  A/m<sup>2</sup>, the two attractors simultaneously collide at the basin boundaries and form a folded chaotic attractor [55], indicating crisis-induced

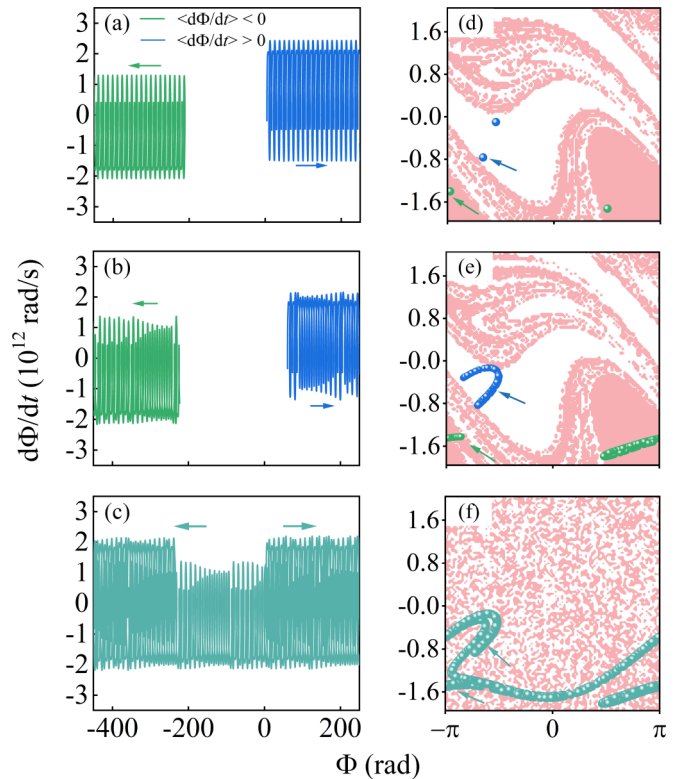


FIG. 4. Trajectories of phase portraits and the basins of attractors under  $J = 4.9 \times 10^{10}$  A/m<sup>2</sup> [(a) and (d)],  $5.04 \times 10^{10}$  A/m<sup>2</sup> [(b) and (e)], and  $5.1 \times 10^{10}$  A/m<sup>2</sup> [(c) and (f)]. The Poincaré sections at  $2\pi f_0 t = 0 \pmod{2\pi}$  under different  $J$  are plotted in (d)–(f). The green and blue trajectories in (a) and (c) denote DW precessions with opposite chirality:  $\langle d\Phi/dt \rangle > 0$  (blue) and  $\langle d\Phi/dt \rangle < 0$  (green). Both running modes are separated in (a), (b), (d), (e) but mixed in (c) and (f).

intermittent chaotic DW precession, which is also verified by the irregular up and down running of  $\Phi$  [Figs. 4(c) and 4(f)].

To experimentally explore chaotic AFM DW precession, the frequency of an alternating current ( $f_0$ ) is generally better to approach the characteristic frequency for DW precession  $f_c = \sqrt{a\gamma^2|D|/\pi\lambda}/4$ , which is hundreds of GHz. This high-frequency current can be transformed from a high-frequency voltage provided by a radio-frequency source [56]. The chaotic oscillation of an AFM Néel vector can be detected by using ultrafast optical methods [57,58].

**Summary.** In summary, we predict the excitation of chaotic AFM DW precession triggered by a spin-polarized current with its polarization along the easy anisotropy axis. This chaos originates from the interfacial DMI of an AFM material and shares the same dynamic equation as a classical pendulum. Our findings unravel rich behaviors of the precessional motion of AFM DWs and paves a way to exploit the magnetization dynamics of AFM textures for developing applicable spintronic devices.

**Acknowledgments.** This study was supported by the National Key Research and Development Program of China (Grant No. 2022YFE0103300) and the National Natural Science Foundation of China (Grants No. 51971098, No. 11734004, No. 12174028, and No. U2141236).

- [1] J. Gleick, *Chaos: Making a New Science* (Open Road Integrated Media, New York, 2011).
- [2] J. H. Xiao, G. Hu, and Z. Qu, *Phys. Rev. Lett.* **77**, 4162 (1996).
- [3] G. Wang, D. Chen, J. Lin, and X. Chen, *IEEE Trans. Ind. Electron.* **46**, 440 (1999).
- [4] G. Z. Li and B. Zhang, *IEEE Trans. Ind. Electron.* **64**, 2255 (2017).
- [5] K. Yang, Q. Duan, Y. Wang, T. Zhang, Y. Yang, and R. Huang, *Sci. Adv.* **6**, eaba9901 (2020).
- [6] S. Kumar, J. P. Strachan, and R. S. Williams, *Nature (London)* **548**, 318 (2017).
- [7] Z. Yang, S. Zhang, and Y. Charles Li, *Phys. Rev. Lett.* **99**, 134101 (2007).
- [8] J. Williams, A. Difini Accioly, D. Rontani, M. Sciamanna, and J. V. Kim, *Appl. Phys. Lett.* **114**, 232405 (2019).
- [9] Z. Li, Y. C. Li, and S. Zhang, *Phys. Rev. B* **74**, 054417 (2006).
- [10] T. Yamaguchi, N. Akashi, K. Nakajima, S. Tsunegi, H. Kubota, and T. Taniguchi, *Phys. Rev. B* **100**, 224422 (2019).
- [11] T. Taniguchi, N. Akashi, H. Notsu, M. Kimura, H. Tsukahara, and K. Nakajima, *Phys. Rev. B* **100**, 174425 (2019).
- [12] L. Chen, K. Zhou, S. Urazhdin, W. Jiang, Y. W. Du, and R. H. Liu, *Phys. Rev. B* **100**, 104436 (2019).
- [13] T. Devolder, D. Rontani, S. Petit-Watelot, K. Bouzehouane, S. Andrieu, J. Létang, M.-W. Yoo, J.-P. Adam, C. Chappert, S. Girod, V. Cros, M. Sciamanna, and J.-V. Kim, *Phys. Rev. Lett.* **123**, 147701 (2019).
- [14] M.-W. Yoo, D. Rontani, J. Létang, S. Petit-Watelot, T. Devolder, M. Sciamanna, K. Bouzehouane, V. Cros, and J.-V. Kim, *Nat. Commun.* **11**, 601 (2020).
- [15] E. G. Tveten, A. Qaiumzadeh, O. A. Tretiakov, and A. Brataas, *Phys. Rev. Lett.* **110**, 127208 (2013).
- [16] R. Cheng, D. Xiao, and A. Brataas, *Phys. Rev. Lett.* **116**, 207603 (2016).
- [17] B. Wolba, O. Gomonay, and V. P. Kravchuk, *Phys. Rev. B* **104**, 024407 (2021).
- [18] O. R. Sulymenko, O. V. Prokopenko, V. S. Tiberkevich, A. N. Slavin, B. A. Ivanov, and R. S. Khymyn, *Phys. Rev. Appl.* **8**, 064007 (2017).
- [19] M. Bode, E. Y. Vedmedenko, K. von Bergmann, A. Kubetzka, P. Ferriani, S. Heinze, and R. Wiesendanger, *Nat. Mater.* **5**, 477 (2006).
- [20] X. Zhang, Y. Zhou, and M. Ezawa, *Sci. Rep.* **6**, 24795 (2016).
- [21] J. Wu, D. Carlton, J. S. Park, Y. Meng, E. Arenholz, A. Doran, A. T. Young, A. Scholl, C. Hwang, H. W. Zhao, J. Bokor, and Z. Q. Qiu, *Nat. Phys.* **7**, 303 (2011).
- [22] H. Jani, J.-C. Lin, J. Chen, J. Harrison, F. Maccherozzi, J. Schad, S. Prakash, C.-B. Eom, A. Ariando, T. Venkatesan, and P. G. Radaelli, *Nature (London)* **590**, 74 (2021).
- [23] E. G. Tveten, A. Qaiumzadeh, and A. Brataas, *Phys. Rev. Lett.* **112**, 147204 (2014).
- [24] T. Shiino, S.-H. Oh, P. M. Haney, S.-W. Lee, G. Go, B.-G. Park, and K.-J. Lee, *Phys. Rev. Lett.* **117**, 087203 (2016).
- [25] O. Gomonay, T. Jungwirth, and J. Sinova, *Phys. Rev. Lett.* **117**, 017202 (2016).
- [26] H. Y. Yuan, W. Wang, M.-H. Yung, and X. R. Wang, *Phys. Rev. B* **97**, 214434 (2018).
- [27] H. Yang, H. Y. Yuan, M. Yan, H. W. Zhang, and P. Yan, *Phys. Rev. B* **100**, 024407 (2019).
- [28] L. Shen, J. Xia, X. Zhang, M. Ezawa, O. A. Tretiakov, X. Liu, G. Zhao, and Y. Zhou, *Phys. Rev. Lett.* **124**, 037202 (2020).
- [29] L. Shen, J. Xia, M. Ezawa, O. A. Tretiakov, G. Zhao, and Y. Zhou, *Appl. Phys. Lett.* **118**, 012402 (2021).
- [30] G. Tatara, C. A. Akosa, and R. M. Otxoa de Zuazola, *Phys. Rev. Res.* **2**, 043226 (2020).
- [31] X. Ge, Y. Chen, Y. Cao, C. Li, T. Li, Z. Li, L. You, S. Liang, X. Yang, and Y. Zhang, *J. Phys. D: Appl. Phys.* **55**, 295302 (2022).
- [32] A. V. Khvalkovskiy, K. A. Zvezdin, Ya. V. Gorbunov, V. Cros, J. Grollier, A. Fert, and A. K. Zvezdin, *Phys. Rev. Lett.* **102**, 067206 (2009).
- [33] W. Lin, J. Cucchiara, C. Berthelot, T. Hauet, Y. Henry, J. A. Katine, Eric E. Fullerton, and S. Mangin, *Appl. Phys. Lett.* **96**, 252503 (2010).
- [34] H. T. Nembach, J. M. Shaw, M. Weiler, E. Jué, and T. J. Silva, *Nat. Phys.* **11**, 825 (2015).
- [35] J.-H. Moon, S.-M. Seo, K.-J. Lee, K.-W. Kim, J. Ryu, H.-W. Lee, R. D. McMichael, and M. D. Stiles, *Phys. Rev. B* **88**, 184404 (2013).
- [36] Md. R. K. Akanda, I. J. Park, and R. K. Lake, *Phys. Rev. B* **102**, 224414 (2020).
- [37] A. Rajanikanth, S. Kasai, N. Ohshima, and K. Ohno, *Appl. Phys. Lett.* **97**, 022505 (2010).
- [38] Z. Lu, R. V. Chepulsii, and W. H. Butler, *Phys. Rev. B* **81**, 094437 (2010).
- [39] See Supplemental Material at <http://link.aps.org/supplemental/10.1103/PhysRevB.107.L020405> for the derivation of the dynamic equations of AFM DWs, atomistic simulations, calculations of Lyapunov exponents, basin of attraction, and the Poincaré section, which includes Refs. [40–50].
- [40] K. M. D. Hals, Y. Tserkovnyak, and A. Brataas, *Phys. Rev. Lett.* **106**, 107206 (2011).
- [41] H. Y. Yuan, Z. Yuan, R. A. Duine, and X. R. Wang, *Europhys. Lett.* **132**, 57001 (2020).
- [42] K. Matsushita, M. Sasaki, and T. Chawanya, *J. Phys. Soc. Jpn.* **81**, 063801 (2012).
- [43] A. Pivano and V. O. Dolocan, *Phys. Rev. B* **93**, 144410 (2016).
- [44] M. Mohseni, Q. Wang, M. Mohseni, T. Brächer, B. Hillebrands, and P. Pirro, *Phys. Rev. Appl.* **13**, 024040 (2020).
- [45] R. F. L. Evans, W. J. Fan, P. Chureemart, T. A. Ostler, M. O. A. Ellis, and R. W. Chantrell, *J. Phys.: Condens. Matter* **26**, 103202 (2014).
- [46] Q. Wang, Y. Yang, and X. Zhang, *Chaos, Solitons & Fractals* **137**, 109832 (2020).
- [47] U. Nowak, *Handbook of Magnetism and Advanced Magnetic Materials* (Wiley, Hoboken, NJ, 2007).
- [48] J. L. García-Palacios and F. J. Lázaro, *Phys. Rev. B* **58**, 14937 (1998).
- [49] S. D. Souza-Machado, R. W. Rollins, D. T. Jacobs, and J. L. Hartman, *Am. J. Phys.* **58**, 321 (1990).
- [50] S. K. Kim, Y. Tserkovnyak, and O. Tchernyshyov, *Phys. Rev. B* **90**, 104406 (2014).
- [51] E. G. Tveten, T. Müller, J. Linder, and A. Brataas, *Phys. Rev. B* **93**, 104408 (2016).
- [52] R. L. Kautz, *J. Appl. Phys.* **58**, 424 (1985).
- [53] A. Ben-Mizrachi, I. Procaccia, N. Rosenberg, A. Schmidt, and H. G. Schuster, *Phys. Rev. A* **31**, 1830 (1985).

- [54] F. Hellman, A. Hoffmann, Y. Tserkovnyak, G. S. D. Beach, E. E. Fullerton, C. Leighton, A. H. MacDonald, D. C. Ralph, D. A. Arena, H. A. Dürr, P. Fischer, J. Grollier, J. P. Heremans, T. Jungwirth, A. V. Kimel, B. Koopmans, I. N. Krivorotov, S. J. May, A. K. Petford-Long, J. M. Rondinelli, N. Samarth, I. K. Schuller, A. N. Slavin, M. D. Stiles, O. Tchernyshyov, A. Thiaville, and B. L. Zink, *Rev. Mod. Phys.* **89**, 025006 (2017).
- [55] E. G. Gwinn and R. M. Westervelt, *Phys. Rev. Lett.* **54**, 1613 (1985); *Phys. Rev. A* **33**, 4143 (1986).
- [56] M. Goto, Y. Wakatake, U. Kalu Oji, S. Miwa, N. Strelkov, B. Dieny, H. Kubota, K. Yakushiji, A. Fukushima, S. Yuasa, and Y. Suzuki, *Nat. Nanotechnol.* **14**, 40 (2019).
- [57] V. Saidl, P. Nemeč, P. Wadley, V. Hills, R. P. Campion, V. Novak, K. W. Edmonds, F. Maccherozzi, S. S. Dhesi, B. L. Gallagher, F. Trojaneč, J. Kunes, J. Zelezny, P. Maly, and T. Jungwirth, *Nat. Photonics* **11**, 91 (2017).
- [58] P. Nemeč, M. Fiebig, T. Kampfrath, and A. V. Kimel, *Nat. Phys.* **14**, 229 (2018).